computation

MDPI

Article

Numerical Analysis of the Impact of Variable Borer Miner Operating Modes on the Microclimate in Potash Mine Working Areas

Lev Levin [1], Mikhail Semin [1,*], Stanislav Maltsev [1], Roman Luzin [1,2] and Andrey Sukhanov [1]

[1] Mining Institute of the Ural Branch of the Russian Academy of Sciences, 614007 Perm, Russia; aerolog_lev@mail.ru (L.L.); st.v.maltsev@ya.ru (S.M.); romeroperm@gmail.com (R.L.); asukhanov@aerologist.ru (A.S.)
[2] Physics and Mathematics Institute, Perm State University, 614007 Perm, Russia
* Correspondence: seminma@inbox.ru

Abstract: This paper addresses the numerical simulation of unsteady, non-isothermal ventilation in a dead-end mine working of a potash mine excavated using a borer miner. During its operations, airflow can become unsteady due to the variable operating modes of the borer miner, the switching on and off of its motor cooling fans, and the movement of a shuttle car transporting ore. While steady ventilation in a dead-end working with a borer miner has been previously studied, the specific features of air microclimate parameter distribution in more complex and realistic unsteady scenarios remain unexplored. Our experimental studies reveal that over time, air velocity and, particularly, air temperature experience significant fluctuations. In this study, we develop and parameterize a mathematical model and perform a series of numerical simulations of unsteady heat and mass transfer in a dead-end working. These simulations account for the switching on and off of the borer miner's fans and the movement of the shuttle car. The numerical model is calibrated using data from our experiments conducted in a potash mine. The analysis of the first factor is carried out by examining two extreme scenarios under steady-state ventilation conditions, while the second factor is analyzed within a fully unsteady framework using a dynamic mesh approach in the ANSYS Fluent 2021 R2. The numerical results demonstrate that the borer miner's operating mode notably impacts the velocity and temperature fields, with a twofold decrease in maximum velocity near the cabin after the shuttle car departed and a temperature difference of about 1–1.5 °C between extreme scenarios in the case of forcing ventilation. The unsteady simulations using the dynamic mesh approach revealed that temperature variations were primarily caused by the borer miner's cooling system, while the moving shuttle car generated short-term aerodynamic oscillations.

Keywords: mine ventilation; heat transfer; computational fluid dynamics; dynamic mesh; dead-end working; potash mine

check for updates

Academic Editors: Ali Cemal Benim, Jeffrey S. Marshall, Sergey A. Karabasov and Dimitris Drikakis

Received: 3 February 2025
Revised: 17 March 2025
Accepted: 19 March 2025
Published: 24 March 2025

Citation: Levin, L.; Semin, M.; Maltsev, S.; Luzin, R.; Sukhanov, A. Numerical Analysis of the Impact of Variable Borer Miner Operating Modes on the Microclimate in Potash Mine Working Areas. *Computation* **2025**, *13*, 85. https://doi.org/10.3390/computation13040085

Copyright: © 2025 by the authors. Licensee MDPI, Basel, Switzerland. This article is an open access article distributed under the terms and conditions of the Creative Commons Attribution (CC BY) license (https://creativecommons.org/licenses/by/4.0/).

1. Introduction

A mine ventilation system is a key element that ensures the uninterrupted operation of a mine and creates safe and comfortable working conditions for miners. In the literature, it is often referred to as the respiratory or circulatory system of the mine [1,2]. However, with increases in production volumes, the rise in harmful emissions, and the complexity of ventilation network structures, fulfilling the primary task of ventilation systems is becoming increasingly difficult [3].

Effective analysis of the branched ventilation networks of mines largely depends on the approaches and methods used to quantify the numerous interconnected physical and technical processes that occur within the mine ventilation system. Organizing effective ventilation at a particular mine usually requires an in-depth scientific study of heat and mass transfer specifics in underground workings, taking into account unique factors characteristic of different types of mines.

For example, for the potash mines of the Starobinskoye and Gremyachinskoye deposits with borer miner extraction, it is important to consider heat emissions from the mining equipment. These heat emissions significantly affect the airflow structure in working areas, as well as the efficiency of diluting and removing harmful impurities from the atmosphere in dead-end workings [4].

The issue of determining the most suitable auxiliary ventilation systems for dead-end workings, as well as the most effective parameters for these systems, is most commonly addressed today using computational fluid dynamics (CFD) methods [5], which are widely recognized as the most efficient for analyzing the three-dimensional structure of airflow and the impurities contained within it, taking into account the geometric features of the working areas.

Researchers use various turbulence models to describe the aerodynamic processes in dead-end workings: the standard k-epsilon model [6], the Realizable k-epsilon model [7,8], the RNG k-epsilon model [9], the Spalart–Allmaras model [10], the Reynolds stress model [11], and others. All of these RANS models are imperfect to some degree, which results in certain discrepancies with experimental data from real mines [12]. Nevertheless, simple semi-empirical models based on the Boussinesq hypothesis can effectively capture the general flow patterns in dead-end mine workings under various mining conditions.

There is also a more complex and less widely recognized approach to mine ventilation problems—the Large Eddy Simulation approach—which is used particularly for analyzing the dynamics of harmful impurities and heat transfer during fires and other emergency situations [13,14]. Its advantage over the RANS models lies in its ability to directly capture large-scale turbulent structures, providing higher accuracy in simulating complex airflow patterns and pollutant dispersion in dynamic and transient scenarios [15]. However, it is much more computationally expensive than the RANS approach.

Currently, numerous studies have been published addressing practical mine ventilation problems through CFD modeling. These studies consider various ventilation systems: forcing [16,17], exhaust [18], and overlap [8,19]. The removal of various harmful substances from dead-end workings is also examined, including gases [20,21], dust [22], particulate matter (PM) [23], and excess heat [24,25]. The presence of different types of mining equipment in the workings is also considered [26,27], although it is often assumed that the working space is not obstructed by equipment. This simplified approach is particularly relevant when ventilating the dead-end face after drilling and blasting operations to remove gases generated by the detonation of explosives [28].

When studying heat and mass transfer processes in dead-end workings excavated using a borer miner (BM), it is essential to consider the impact of mining machinery—both in terms of the congestion they create in the working space and the aerodynamic and thermal effects they generate. The significance of these factors has been experimentally and theoretically demonstrated in our previous studies [4,29]. However, these studies were conducted under steady-state conditions, while in practice, the data from our monitoring of the microclimatic air parameters in the working areas of potash mines show that mining equipment is in motion during operation, which creates significant local disturbances in airflow and temperature fields. This is primarily related to the dynamics of the shuttle car

transporting ore from the BM to the conveyor, and the switching on/off of the BM's engine cooling system.

The dynamics of transportation in mine workings can only be solved numerically using a dynamic mesh approach [30]. This approach has previously been applied in the mining literature to study the dynamics of hoisting vessels in vertical mine shafts [31], as well as the dynamic advancement of the face during underground tunnel excavation [32]. The effect of periodic movements of mining machinery and the periodic shutdowns of the machinery's ventilation system has not been addressed in the literature. The present study is dedicated to investigating this issue.

2. Materials and Methods

2.1. Object of Study

The object of this study is the airspace of a dead-end mine working, traversed by a periodically operating BM and a moving shuttle car. The basic layout of a dead-end mine working and the mining equipment within it are illustrated in Figure 1. Two auxiliary ventilation systems were analyzed in this study: a forcing system (Figure 1a) and an exhaust system (Figure 1b). In a forcing ventilation system, fresh air is supplied through ventilation duct No. 1, located on the left side (when looking at the working face) at the top of the mine working. In an exhaust ventilation system, fresh air is supplied through the mine working itself, while exhaust air is removed through ventilation duct No. 2, positioned on the right side at the floor of the mine working. Consequently, at any given time, only one ventilation duct—either No. 1 or No. 2—is installed in the dead-end working. Ventilation duct No. 1 has a diameter of 0.78 m, while ventilation duct No. 2 has a diameter of 0.6 m. Despite the different diameters, the airflow rates in the ducts are assumed to be equal in absolute value.

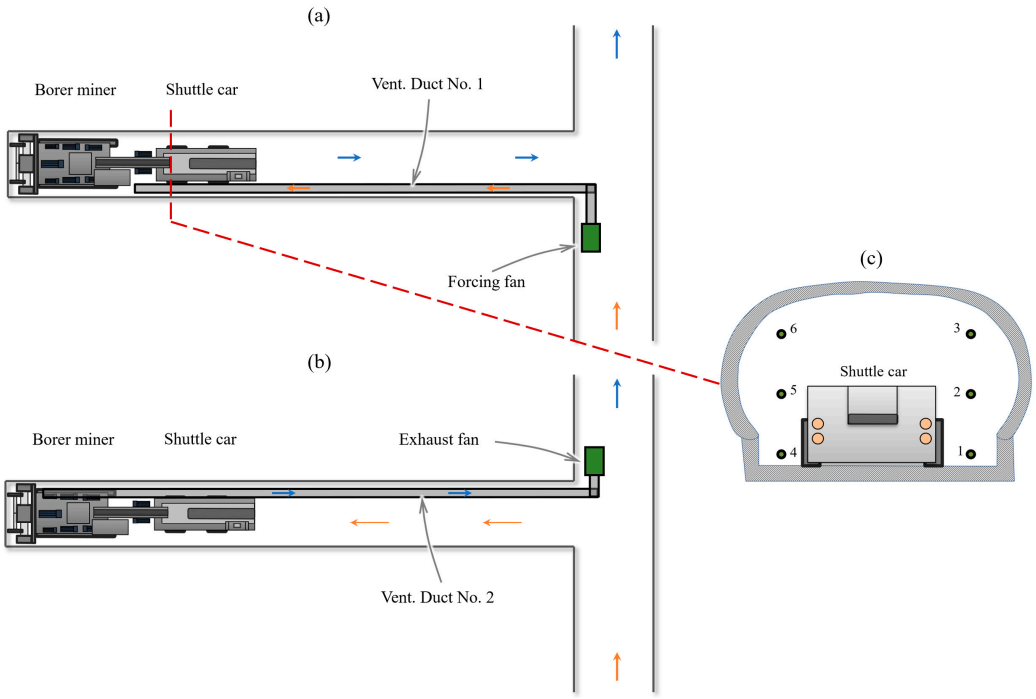

Figure 1. Layout of mining equipment in cases of forcing (**a**) and exhaust (**b**) ventilation systems; grid of measurement points 1–6 in the cross-section of a mine working (**c**).

A key aspect of the study was the mobility of the shuttle car, which forms an integral part of the technological cycle for mineral extraction and transportation. The shuttle car periodically travels between the BM and the conveyor (located outside the dead-end

working and not included in the model), unloads ore at the conveyor, and then returns to the BM. The mean velocity of the shuttle car (2.5 m/s) and the acceleration time (0.5 s) required to reach this velocity from rest are based on the vehicle's performance characteristics.

The geometric parameters of the dead-end working and the mining equipment present in it (see Figure 2) were determined based on preliminary experimental studies conducted in a dead-end mine working at a potash mine located in Russia. These experimental studies also served to validate the heat and mass transfer model.

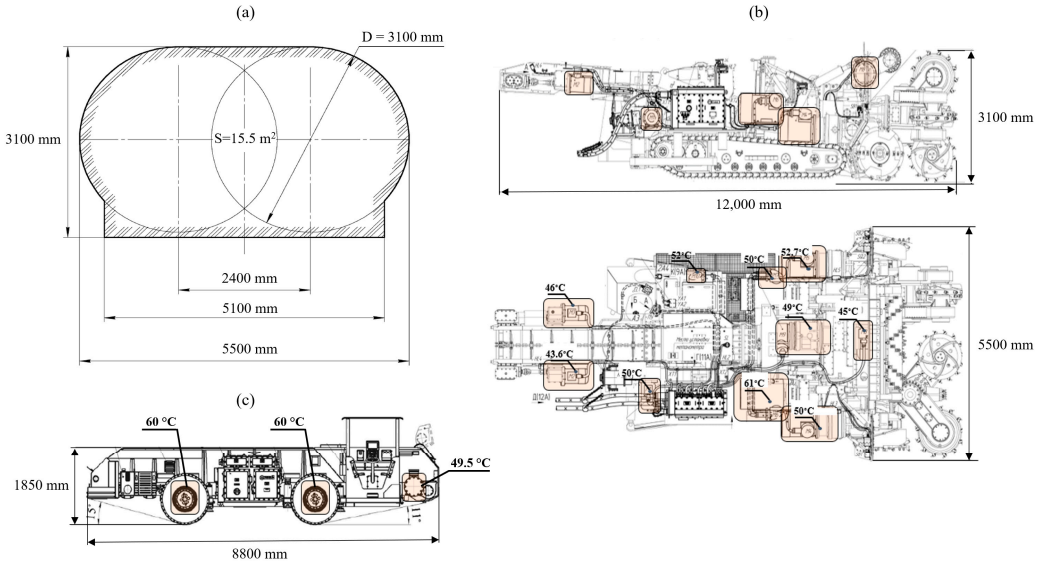

Figure 2. Geometric parameters of the mine working (**a**) and the mining equipment within it: BM (**b**) and shuttle car (**c**).

The length of the dead-end working is 50 m, with a cross-sectional area of 15.5 m^2, as shown in Figure 2a. The airflow rate at the outlet of the ventilation duct (for the forcing ventilation system) is 4.06 m^3/s. A similar airflow rate is drawn into the ventilation duct for the exhaust ventilation system.

2.2. Experimental Measurement Methodology

Experimental studies of air velocity were conducted for the forcing ventilation system in the cross-section shown in Figure 1. Measurements were taken at various heights, with the measurement scheme illustrated in Figure 1c. In addition to detailed point-by-point measurements of air velocity in the specified section, the average air velocity at the end of the ventilation duct was measured, along with a verification measurement of the average air velocity at the mouth of the dead-end working.

The velocity at each point was measured using an APR-2 anemometer (Ecotechinvest, Moscow, Russia) with an absolute error equal to $0.03 + 0.02V$ (m/s), where V is the measured value of air velocity (m/s). For each point, the velocity was measured continuously for 1 min, after which the time-averaged value was calculated. It is important to note that during the measurements, the BM was operating with nominal power.

Air temperature measurements were also conducted in the section shown in Figure 1c at six points near the shuttle car (2 m behind the BM operator's cabin). Additionally, air temperature was measured at the mouth of the dead-end working and at the outlet of the ventilation duct. Temperature measurements were performed using a portable Fluke 971 thermo-hygrometer (Fluke Corporation, Washington, DC, USA). Long-term air temperature measurements were carried out using a Kestrel D3 sensor (Nielsen-Kellerman, Boothwyn, PA, USA), while surface temperatures were recorded with a Fluke infrared thermometer and a Hikmicro G60 thermal imager (Hikmikro, Hangzhou, China).

2.3. Mathematical Model and Its Numerical Implementation

The heat and mass transfer problem in the atmosphere of a dead-end working was solved numerically by addressing the system of Reynolds-averaged Navier–Stokes (RANS) equations, which represent the conservation laws of mass, momentum, and energy:

$$\frac{\partial \rho}{\partial t} + \frac{\partial}{\partial x_i}(\rho u_i) = 0 \tag{1}$$

$$\rho\left(\frac{\partial u_i}{\partial t} + u_j\frac{\partial u_i}{\partial x_j}\right) = -\frac{\partial}{\partial x_i}\left[p + \frac{2}{3}\left(\rho k + \mu_{eff}\frac{\partial u_j}{\partial x_j}\right)\right] + \frac{\partial}{\partial x_j}\left[\mu_{eff}\frac{\partial u_i}{\partial x_j}\right] + \rho g_i \tag{2}$$

$$\frac{\partial(\rho e)}{\partial t} + \frac{\partial}{\partial x_i}[u_i(\rho e + p)] = \frac{\partial}{\partial x_j}\left[\lambda_{eff}\frac{\partial T}{\partial x_j} + u_i\left(\mu_{eff}\frac{\partial u_i}{\partial x_j}\right)\right] \tag{3}$$

$$e = c_p(T - T_0) - \frac{p}{\rho} + \frac{u_i u_i}{2} \tag{4}$$

$$\lambda_{eff} = \lambda + \frac{c_p \mu_{turb}}{Pr_t} \tag{5}$$

where ρ is the air density, in kg/m^3; u_i is the air velocity vector, in m/s; p is the pressure in Pa; $\mu_{eff} = \mu + \mu_t$ is the effective dynamic viscosity of the air, in Pa·s; μ is the molecular viscosity of the air, in Pa·s; μ_t is the turbulent viscosity of the air, in Pa·s; k is the turbulent kinetic energy, in m^2/s^2; g_i is the gravity acceleration vector, in m/s^2; e is the specific total energy of the air, in J/kg; c_p is the specific heat capacity of the air, in J/(kg·°C); λ_{eff} is the effective heat conductivity of the air, in W/(m·°C); λ is the air heat conductivity due to molecular transport, in W/(m·°C); T is the air temperature, in °C; T_0 is the reference air temperature, in °C; and Pr_t is the turbulent Prandtl number.

The dependence of air density on temperature was taken into account using the Mendeleev–Clapeyron equation:

$$\rho = \frac{p}{R(T + 273.15)} \tag{6}$$

where R is the gas constant of air, in J/(kg·°C).

The closure of the system of Equations (1)–(6) was carried out using the Boussinesq hypothesis and the Realizable k-ε turbulence model. This choice was based on a preliminary comparison of this model with other two-parameter models. The Realizable k-ε model showed better values for residuals during preliminary simulations. As follows from [33], this model is suitable for jet flows, flows with separation, or moderate swirl.

$$\frac{\partial}{\partial t}(\rho k) + \frac{\partial}{\partial x_j}(\rho k u_j) = \frac{\partial}{\partial x_j}\left[\left(\mu + \frac{\mu_t}{\sigma_k}\right)\frac{\partial k}{\partial x_j}\right] + G_k + G_b - \rho\varepsilon \tag{7}$$

$$\frac{\partial}{\partial t}(\rho\varepsilon) + \frac{\partial}{\partial x_j}(\rho\varepsilon u_j) = \frac{\partial}{\partial x_j}\left[\left(\mu + \frac{\mu_t}{\sigma_\varepsilon}\right)\frac{\partial \varepsilon}{\partial x_j}\right] + \rho C_1 S\varepsilon - \rho C_2\frac{\varepsilon^2}{k + \sqrt{\frac{\mu\varepsilon}{\rho}}} + C_{1\varepsilon}\frac{\varepsilon}{k}C_{3\varepsilon}G_b \tag{8}$$

$$C_1 = max\left[0.43, \frac{\eta}{\eta + 5}\right], \quad \eta = S\frac{k}{\varepsilon}, \quad S = \sqrt{2S_{ij}S_{ij}} \tag{9}$$

$$G_k = \mu_t S^2 \tag{10}$$

where ε is the rate of dissipation of kinetic energy, in m^2/s^3; G_k is the generation of turbulent kinetic energy due to average velocity gradients, in kg/(m·s^2); G_b is the generation of turbulence kinetic energy due to buoyancy, in kg/(m·s^2); σ_k and σ_ε are turbulent analogues

of the Prandtl number; S is the invariant of the tensor S_{ij} of flow deformation rates, in s^{-1}; and C_1, $C_{1\varepsilon}$, C_2, and $C_{3\varepsilon}$ are empirical coefficients of the model.

Within the framework of the chosen turbulence model, turbulent viscosity μ_t was determined by the following formulae:

$$\mu_t = \rho \frac{1}{A_0 + A_s \frac{kU^*}{\varepsilon}} \frac{k^2}{\varepsilon} \tag{11}$$

$$U^* \equiv \sqrt{S_{ij}S_{ij} + \tilde{\Omega}_{ij}\tilde{\Omega}_{ij}} \tag{12}$$

$$A_s = \sqrt{6}\cos\varphi, \varphi = \frac{1}{3}\cos^{-1}\left(\sqrt{6}W\right) \tag{13}$$

$$W = \frac{S_{ij}S_{jk}S_{ki}}{\tilde{S}^3} \tag{14}$$

where $\tilde{\Omega}_{ij}$ is the tensor of the average rotation velocity, in a rotating reference frame taking into account angular velocity; $A_0 = 4.04$ is the model parameter.

The system of Equations (1)–(14) was supplemented with boundary and initial conditions. Zero-velocity boundary conditions were applied to the walls of the working area, ventilation duct, and machinery. Exceptions were made for the solid surfaces inside the engines of the BM and shuttle car, where a fixed tangential air velocity was specified to account for engine blow-off.

A velocity inlet boundary condition was applied at the inlet to the computational domain. For a forcing ventilation system, the inlet was located at the end of ventilation duct No. 1, while for an exhaust ventilation system, the inlet was positioned at the mouth of the dead-end working (see Figure 1).

A zero-excess pressure condition was applied at the outlet of the computational domain. For a forcing ventilation system, the outlet was located at the mouth of the dead-end working, whereas for an exhaust ventilation system, the outlet was positioned at the end of ventilation duct No. 2 (see Figure 1).

In addition to aerodynamic boundary conditions, thermal boundary conditions were also applied. The uniform temperature of the walls of the mine working was selected to achieve the best agreement with in situ measurement data from the mine and was set to 37.5 °C. The air temperature at the inlet was set to 38.8 °C for the forcing ventilation system and 37.5 °C for the exhaust ventilation system. A zero-heat-flux condition was assumed for the walls of ventilation ducts No. 1 and No. 2, as well as for the BM and shuttle car.

For calculations involving a dynamic mesh, it was necessary to establish initial conditions. These were based on the results of a steady-state heat and mass transfer simulation for the domain, corresponding to the state before the shuttle car began moving from the BM to the mouth of the dead-end working.

The numerical solution of the system of Equations (1)–(14) was obtained using the finite volume method. The computational domain was discretized into tetrahedral cells in the interior region and prismatic layers near solid walls, where the no-slip velocity condition was applied. A tetrahedral mesh was chosen over a polyhedral one due to its greater flexibility in configuring dynamic mesh setups. Mesh convergence analysis was performed to determine optimal parameters for the numerical mesh, ensuring both solution accuracy and independence from the domain discretization method.

In our calculations, convergence was defined by absolute residuals: 1×10^{-4} for the Navier–Stokes equations and turbulent transport equations and 1×10^{-6} for the energy

equation. We also monitored the attainment of steady-state values for the mean and maximum velocities in selected cross-sections of the domain.

A comparison of three different meshes, evaluated based on two criteria—average velocity and air temperature in the cross-section of the BM operator's cabin—is presented in Table 1. The results indicate that the coarse mesh satisfies all required conditions and is suitable for further calculations. Additional mesh refinement does not significantly affect the key characteristics but considerably increases the computational time required to obtain the numerical solution.

Table 1. Mesh convergence of the model.

Number of Cells	Average Air Velocity Near the BM Operator's Cabin, m/s	Average Air Temperature Near the BM Operator's Cabin, °C
2,892,830	1.304	39.46
3,230,783	1.321	39.45
3,717,122	1.300	39.44

For the selected mesh, the maximum value of the $Y+$ parameter was approximately 73.2. Figure 3 provides a view of the discretized computational domain, showing (Figure 3a) the mouth of the dead-end working and (Figure 3b) a cross-section through the vertical median plane of the dead-end working. The selected mesh consists of 3,230,783 cells and was used for subsequent simulation.

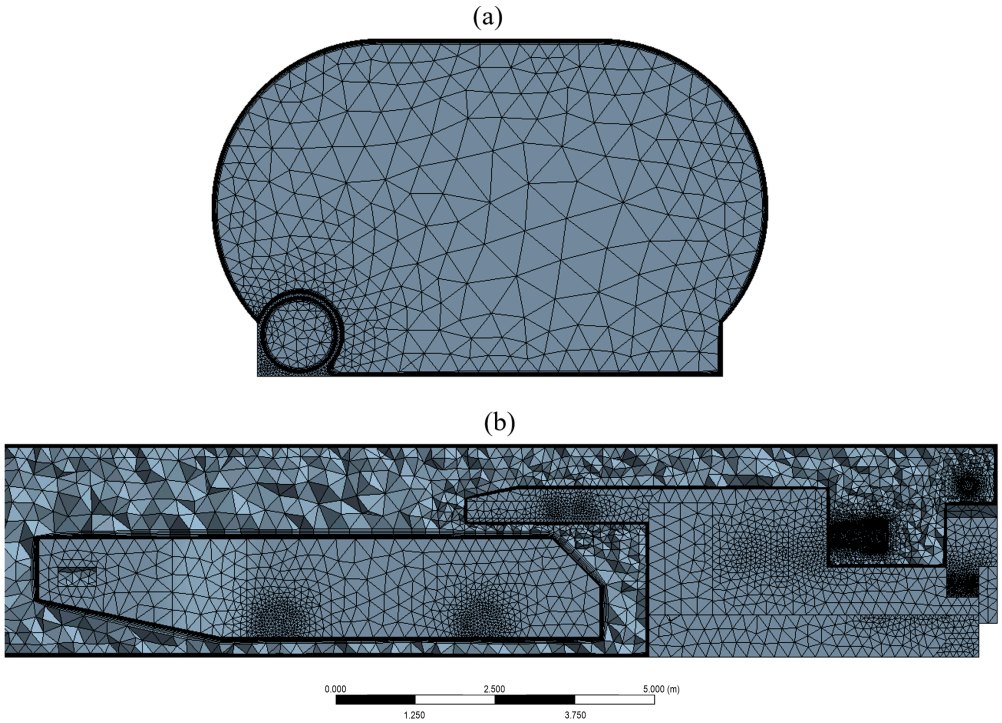

Figure 3. Computational mesh: view from the mouth of a dead-end working (**a**) and view in transverse median vertical section (**b**).

The main parameters of this mesh are as follows: the size of the tetrahedral cells nearest to the walls of the dead-end working is 0.2 m, while the size of the tetrahedral cells closest to the ducts is 0.07 m. The cell size on the surfaces of the mining equipment (excluding engine blower systems) is 0.25 m. For the walls of the engine blower systems, the minimum size of the tetrahedral cells is 0.02 m. On all walls with a no-slip velocity condition, 10 layers of prismatic cells were specified, with the first layer having a thickness

of no more than $2 \cdot 10^{-3}$ m. The mesh had the following quality properties: an average element quality of 0.41, an average skewness of 0.25, and an average orthogonal quality of 0.73.

3. Results and Discussion

3.1. Model Validation

First, the mathematical model was validated using data from a full-scale experiment. The measured values of temperature and air velocity in the section shown in Figure 1c were used for validation. Figure 4 compares the vertical profiles of air velocity along the axis of the dead-end working, based on numerical simulation results and experimental data (measurement points 1–6). The average measured values and their variability, determined from a sample of measurements, are shown for the experimental points. This variability is associated with the unsteady mass transfer processes in the dead-end working, caused by technological factors such as the sloshing of a flexible duct, movement, and falling of ore from the BM's boom, among others.

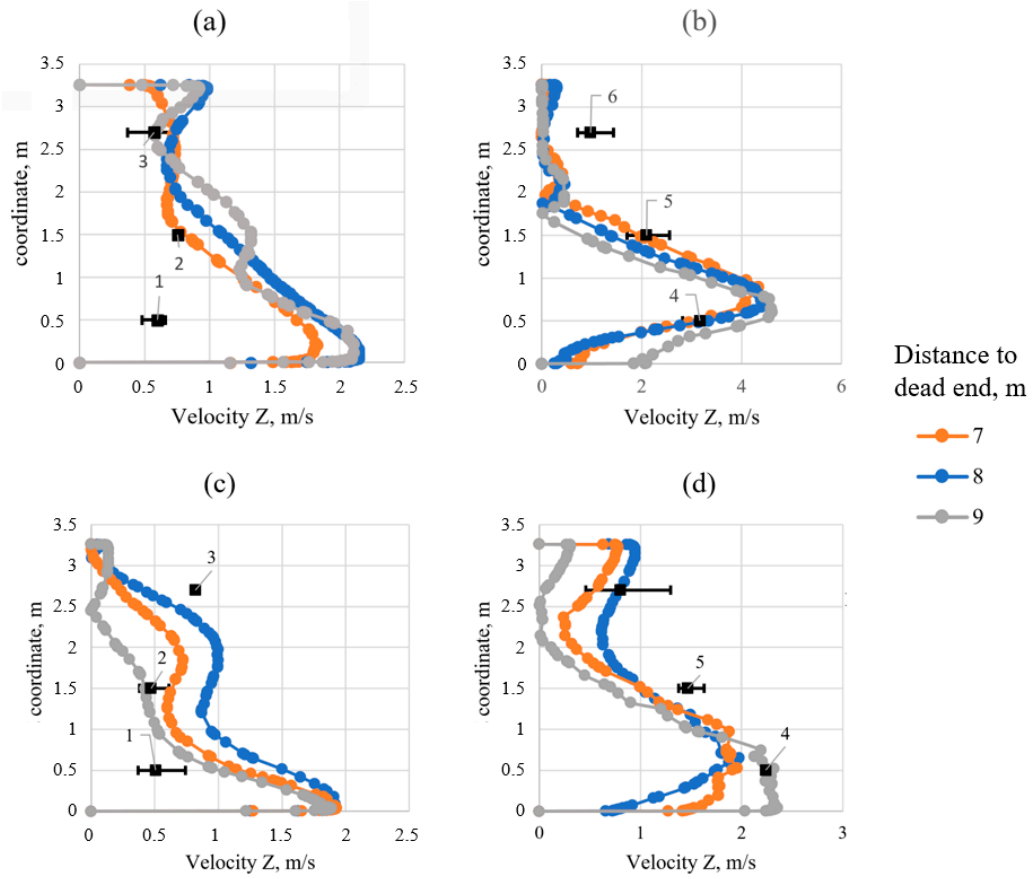

Figure 4. Comparison of theoretical dependences of air velocity on vertical coordinate with experimental points in the situation with a shuttle car (**a**,**b**) and without it (**c**,**d**); to the right of the shuttle car (**a**,**c**) and to the left of the shuttle car (**b**,**d**).

Two extreme scenarios are considered: (1) the presence of a shuttle car near the BM when the latter is switched on (Figure 4a,b), and (2) the absence of a shuttle car near the BM when it is switched off (Figure 4c,d). In general, considering two steady-state calculations corresponding to extreme scenarios significantly sped up the model adjustment procedure, as steady-state calculations are much faster than transient ones.

The model accurately reproduces the experimental data for airflow to the left of the cabin (near the duct), showing agreement in both average velocities and the general upward

trend from the top to the bottom. However, to the right of the cabin, while the overall airflow rate is preserved, the velocity profile in the model is slightly less uniform. A higher velocity field is observed near the dead-end working bottom compared to the experiment. This discrepancy may be attributed to numerical error, measurement instrument error, or the omission of minor geometric details when developing the model of the dead-end working with the BM and shuttle car.

The model also effectively captures the general changes in air distribution associated with the movement of the BM. This is particularly evident in Figure 4b,d, where the difference in average flow velocities between the scenarios with and without the shuttle car is pronounced.

In the presence of a shuttle car, the air stream leaving duct No. 1 is more constrained and expands more slowly. As a result, Figure 4b shows higher peak velocities at the bottom of the dead-end working (approximately 4.5 m/s), whereas Figure 4d shows significantly lower peak velocities. Figure 5 illustrates the streamlines of the airflow interacting with the shuttle car and ventilating the dead-end working containing a BM and shuttle car.

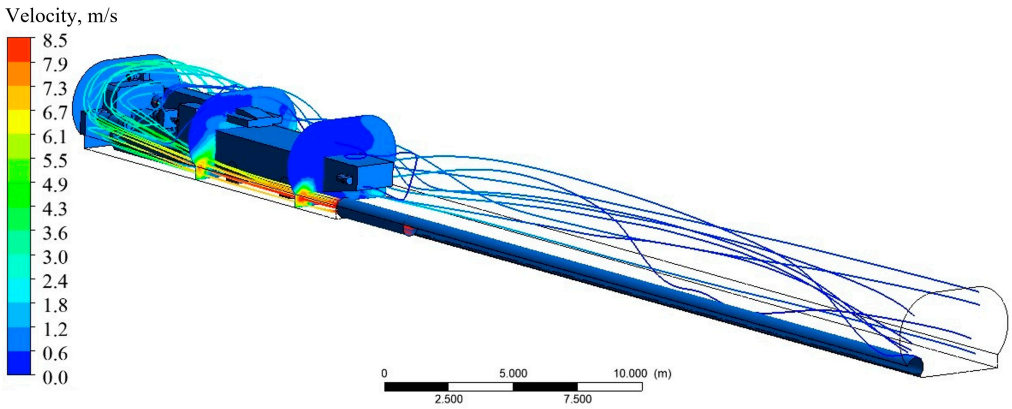

Figure 5. Air velocity streamlines in a dead-end working with a BM and a shuttle car—forcing ventilation system.

From Figure 5, it is evident that the peak air velocities in the cross-section of the dead-end working near the front edge of the shuttle car exceed 6.7 m/s. This indicates that the air stream, which has a velocity of 8.5 m/s at the exit from the ventilation duct, decreases by only 20–25% after approximately 10 m (equivalent to 16 typical duct diameters). Notably, immediately behind this cross-section lies the operator's cabin. When entering or exiting the cabin, the operator is exposed to this high-speed air jet, which somewhat disrupts workplace comfort.

This issue highlights the importance of considering alternative ventilation systems. While the forcing system is currently analyzed, the potential for implementing an exhaust ventilation system will be addressed later in this section.

Popular indicators for estimating the integral error of a model are the MAE and RMSE metrics, which are based on summing the errors (differences between model and experimental values) at individual points. These indicators are convenient for checking the convergence between a numerical model and experimental results. To calculate the mean absolute error (MAE) and the root mean square error (RMSE), samples are taken from the average values of three measurements at experimental points (y_i^*) and the average values at corresponding points in the numerical model (y_i). For a more convenient assessment, relative values are considered instead of absolute deviations.

$$MAE = 100\% \cdot \frac{1}{n} \sum_{i=1}^{n} \left| \frac{y_i - y_i^*}{y_i^*} \right| \quad (15)$$

$$RMSE = 100\% \cdot \sqrt{\frac{1}{n}\sum_{i=1}^{n}\left(\frac{y_i - y_i^*}{y_i^*}\right)^2} \quad (16)$$

where n is the sample length.

Table 2 presents the error values for two extreme situations for which the steady-state calculation was carried out. The average model error for velocities does not exceed 7%, and the root mean square error does not exceed 8%.

Table 2. Estimation of the integral error of the model in predicting the velocity field.

Situation	MAE, %	RMSE, %
With shuttle car	7	8
Without shuttle car	6	2

When validating the model for temperatures, we compared the measured and calculated temperatures near the BM operator's cabin. During the experimental studies, we were able to capture the temporal trend of the temperature in the area of the operator's cabin (see Figure 6). The peak values (39.9 °C) correspond to the period when the BM was on and the shuttle car was near it. The minimum values (38.6–38.8 °C) correspond to the period when the BM was off and the shuttle car was absent from the dead-end working. These values were used to adjust the model.

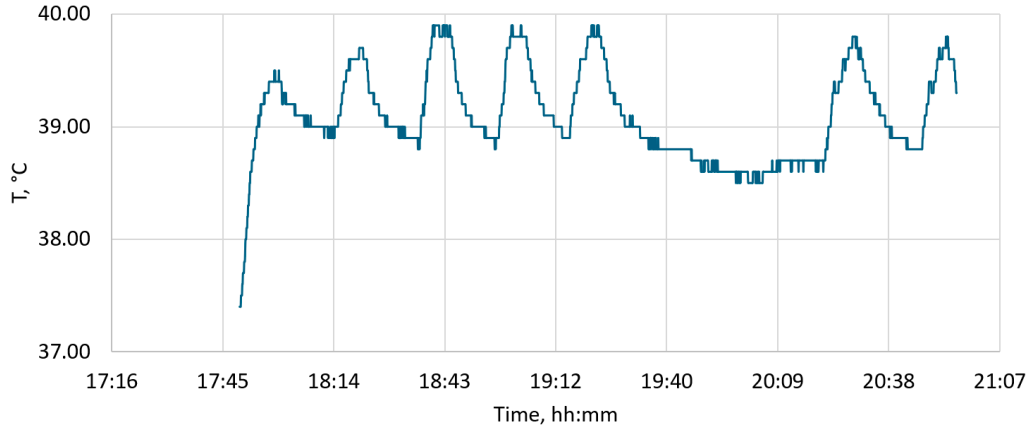

Figure 6. Time dependence of temperature near the BM cabin during mining operations.

Table 3 shows the calculated air temperatures at the location corresponding to the measurement point. To adjust the model, various assumptions were made about the nature of heat transfer through the duct wall (e.g., thermal insulation or a fixed wall temperature), and different values of the turbulent Prandtl number were tested. Overall, the analysis indicates that the model reproduces the measured temperature field quite well across all scenarios. Additionally, the measured and calculated air temperatures at the mouth of the dead-end working were compared.

The model with a turbulent Prandtl number of 0.7 showed better agreement with the field observation data in the cross-section of the dead-end working at its mouth and was selected for further numerical simulations. The model with a lower Prandtl number produced a more uniform temperature field at the working mouth, aligning more closely with the observed data. Additionally, the model with a turbulent Prandtl number of 0.7 demonstrated better convergence.

Table 3. Comparison of the temperature in the BM driver's cabin under different conditions.

Situation	Pr_t	Temperature, °C	
		Duct	Cabin
With shuttle car	0.85	Insul.	39.9
	0.85	38.8	40.0
	0.7	38.8	39.9
Without shuttle car	0.85	Insul.	38.9
	0.85	38.8	-
	0.7	38.8	38.8

In general, although it is traditionally believed that the turbulent Prandtl number should be around 0.85 for air [34], studies have shown that it is non-uniformly distributed across the cross-section of turbulent flow regions [35,36]. It can vary by more than 20% from this average value, depending on the Reynolds number and the turbulent Peclet number of the flow.

3.2. Comparison of Forcing and Exhaust Ventilation Systems

A verified and validated numerical model of a dead-end mine working ventilated using a forcing system was employed to analyze the heat and mass transfer characteristics in the case of an exhaust system. The main difference between the exhaust system and the forcing system is that, in the exhaust system, air is directed from the mouth of the mine working towards its face and is removed through ventilation duct No. 2, located on the opposite side of the BM. This significantly alters the flow structure in the mine working (see Figure 7). Unlike the active mixing of flows in a turbulent vortex observed with the forcing ventilation system, the exhaust system primarily facilitates advective heat and mass transfer. This offers prospects for zonal ventilation of the dead-end mine working.

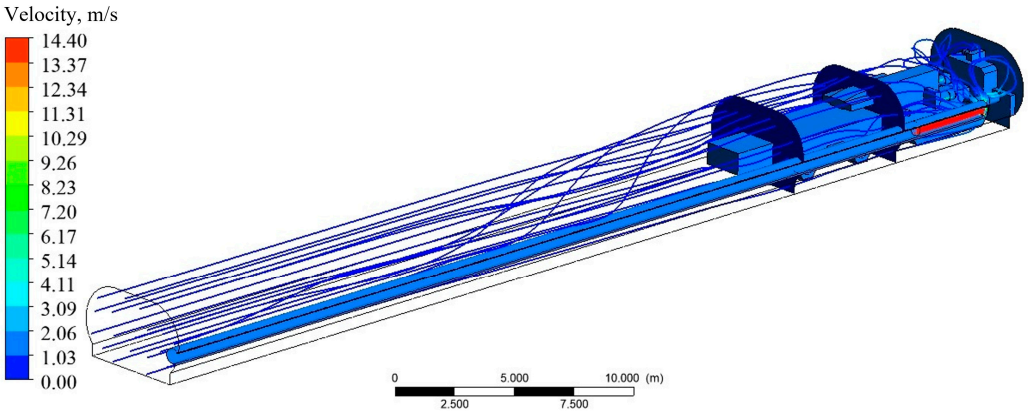

Figure 7. Air velocity streamlines in a dead-end working with a BM and a shuttle car—exhaust ventilation system.

The equipment layout for the exhaust system is similar to that of the forcing system, as shown in Figure 1b. The difference is that air is removed from the face through the duct instead of being supplied, thereby reversing the direction of airflow in the working. Also, duct No. 2 has a slightly smaller diameter (0.6 m). A key requirement for implementing the exhaust system is maintaining appropriate duct lag distances from the BM shield, depending on the airflow rate in the dead-end working.

From a modeling perspective, it is advisable to consider the worst-case parameters, characterized by the highest air velocity. This approach ensures that air exiting the coolers in the face area leaves the working space more rapidly toward the face. The duct lag from

the BM shield is set to 2.0 m. For a more accurate comparison of this system, calculations are conducted using the same airflow rate as in the forcing ventilation system.

Figure 8 shows the results of calculating the temperature field in a dead-end working for two different ventilation systems and for two extreme situations.

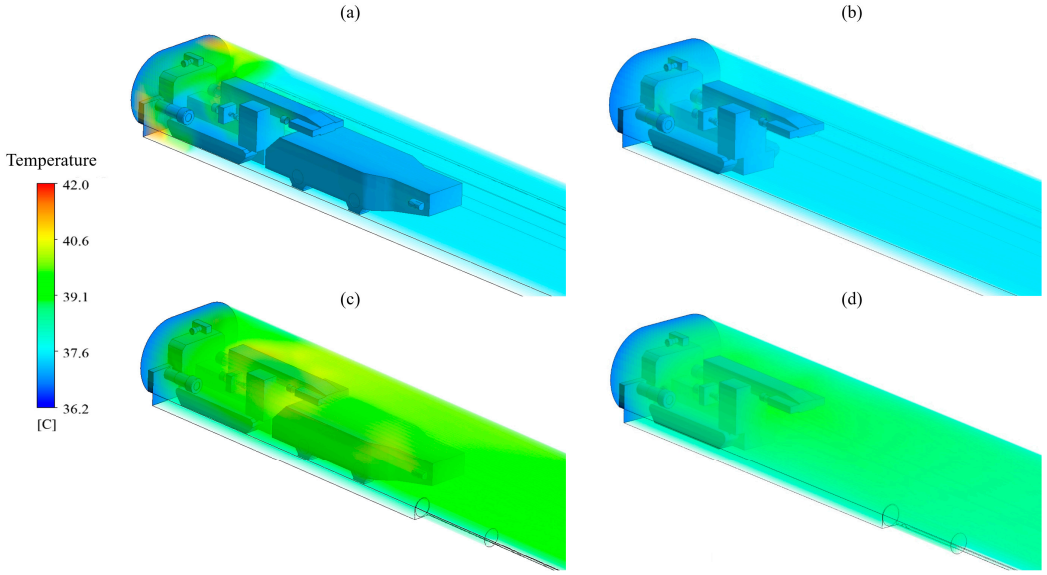

Figure 8. Volumetric temperature fields for the operating BM with a shuttle car (**a**,**c**) and the shut-off BM without a shuttle car (**b**,**d**), in an exhaust ventilation system (**a**,**b**) and a forcing ventilation system (**c**,**d**).

It is evident from the figure that the use of the exhaust system significantly reduces air temperature in most of the dead-end working, particularly in the area of the BM cabin. Air temperatures in this area decrease almost to the temperature of the fresh air stream (see Figure 9). This pronounced decrease (by 2 °C to 4 °C) is attributed to two factors: (1) the air stream entering the dead-end working is not heated by the auxiliary fan, and (2) the air stream is heated by the BM cooling system downstream of the BM cabin.

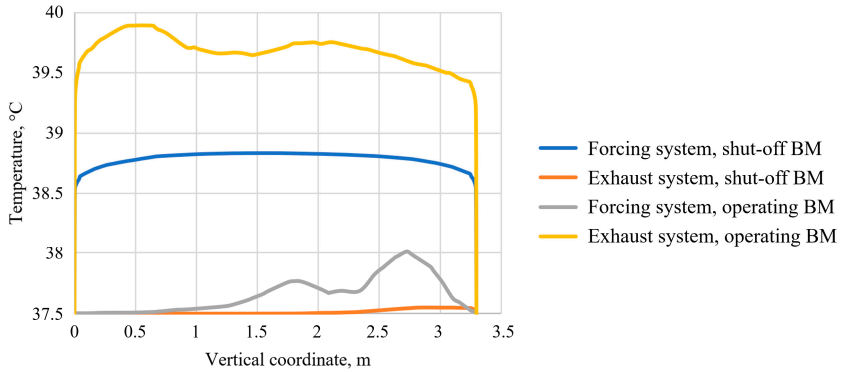

Figure 9. Temperature profiles along the vertical line near the BM cabin for two ventilation options and for two scenarios.

Additionally, the exhaust system is advantageous in terms of maintaining comfortable microclimatic conditions near the BM cabin. The average air velocity in this area is less than 0.5 m/s, as shown in Figure 7. Of course, working conditions, even at a temperature of 37.5 °C, cannot be described as comfortable. However, it is important to highlight that the exhaust system does not cause additional heating of the air before it reaches the workplace. Introducing a colder air stream into the dead-end working could potentially lower the temperature to the required levels, but this aspect is beyond the scope of the current study.

3.3. Unsteady Simulation Within the Dynamic Mesh Approach

Based on the aforementioned analysis of two extreme ventilation scenarios in a dead-end mine working, a conclusion was drawn regarding the significance of the variable operating modes of mining equipment. Moreover, variations in both the velocity field and the temperature field are significant. To study the transition from one scenario to another in greater detail, we adopted a fully unsteady formulation and examined changes in heat emissions from the BM as well as the movement of the shuttle car.

We applied the dynamic mesh approach to analyze the effect of shuttle car movement on air velocity and temperature fields in a dead-end mine working. The shuttle car's movement speed was set at approximately 2.5 m/s based on its specifications. Acceleration and deceleration were modeled to occur within 0.5 s. The mesh deformation was carried out using a combination of smoothing and remeshing methods. Every two time steps in the numerical calculation, the mesh was rebuilt around the moving shuttle car. In this process, only the tetrahedral elements near the moving object were reconstructed to expedite the remeshing procedure. The maximum asymmetry of the cells was predefined to control the desired mesh quality.

Spring-based smoothing was used to smooth the deforming mesh. This method treats the mesh edges between nodes as interconnected springs with defined stiffness [37,38]. The Spring Constant Factor was set to 0.1. This value determines where the mesh will predominantly deform. The lower the value, the closer to the moving boundary the cells will deform.

The 'Tet in Mixed Zones' setting is enabled, allowing only tetrahedrons to deform without affecting the prismatic elements in the boundary layer [39].

The cells corresponding to the boundary layers of the shuttle car and the mine walls were neither deformed nor reconstructed during the numerical calculations. Instead, the boundary layer cells of the shuttle car moved along with it as a single non-deformable solid body.

Figure 10 shows the median vertical section of the finite-volume mesh at different time points. Figure 10a represents the initial state, Figure 10b corresponds to 2 s, and Figure 10c to 4 s. The figure illustrates how the mesh is reconstructed during the calculation process while preserving the approximate characteristic cell size in the area vacated by the shuttle car.

Figures 11 and 12 illustrate the changes in the velocity field over time for both the forcing and exhaust ventilation systems. The figures show that in both cases, the velocity field undergoes significant changes as the shuttle car moves away from the BM. However, the temperature field remains nearly unchanged during the first few seconds after the shuttle car starts moving. For the forcing system, the displacement of the shuttle car causes short-term changes in the shape of a large-scale vortex circulating in the dead-end zone, which is created by a high-speed jet exiting from duct No. 1. For the exhaust system, the velocity field changes significantly, primarily in the vicinity of the moving shuttle car itself.

The simulation results show that only minor temperature fluctuations occur during the shuttle car's travel time (see Figure 13). Figure 8 shows that the temperature field remains relatively uniform, especially in the case of a forcing ventilation system. This is likely due to the influence of a large vortex circulating within the mine working, which actively mixes the air. Consequently, the piston effect of the shuttle car alone does not create a qualitatively different temperature field unless accompanied by the exhaust of a substantial additional heat volume.

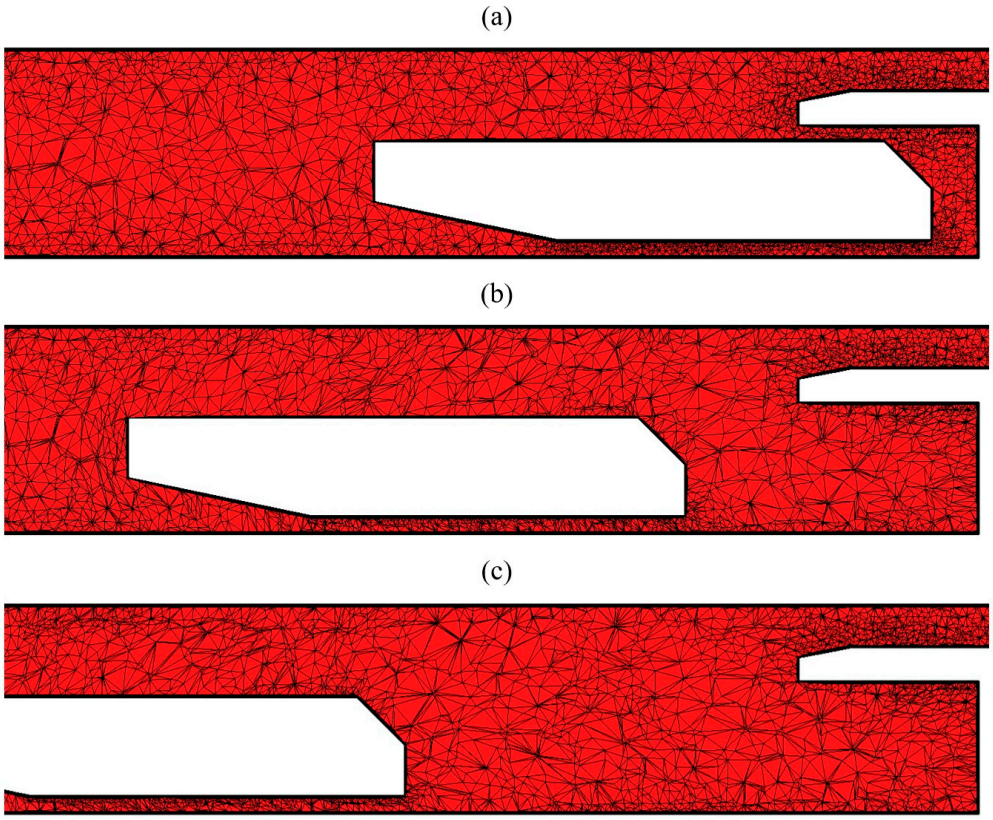

Figure 10. Finite-volume mesh at different time moments: 0 s (**a**), 2 s (**b**), 4 s (**c**).

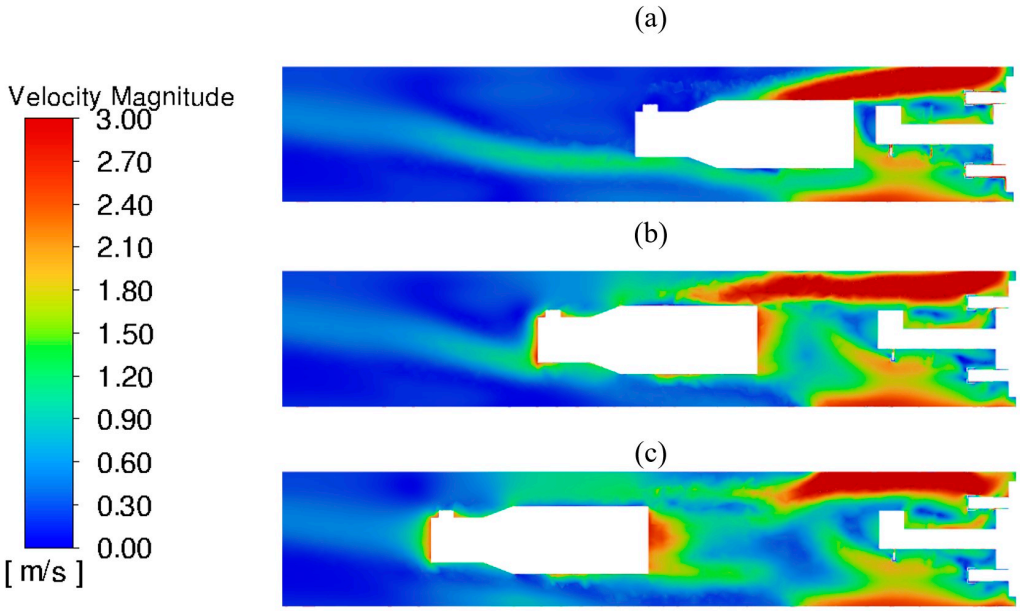

Figure 11. Air velocity fields in the middle horizontal section of a dead-end working at different time moments: 0 s (**a**), 2 s (**b**), 4 s (**c**); forcing ventilation system.

Another thermal factor is the changing heat emission from the BM and the shuttle car. However, the shutdown of the BM cooling system has not yet affected the air temperature in the dead-end working, as insufficient time has passed for complete or near-complete air exchange within the studied domain.

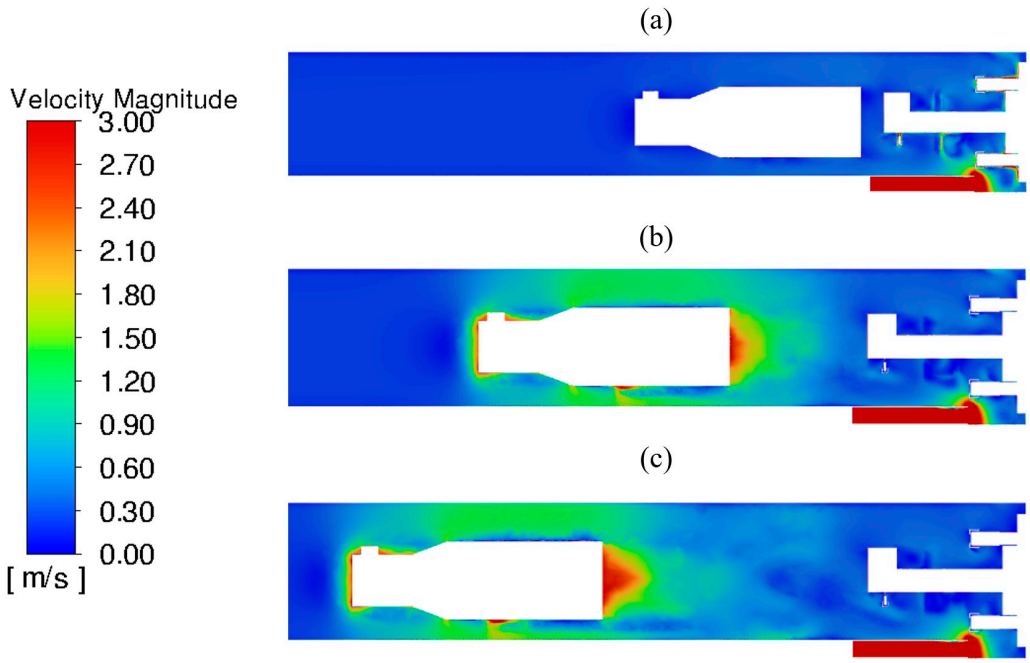

Figure 12. Air velocity fields in the middle horizontal section of a dead-end working at different time moments: 0 s (**a**), 2 s (**b**), 4 s (**c**); exhaust ventilation system.

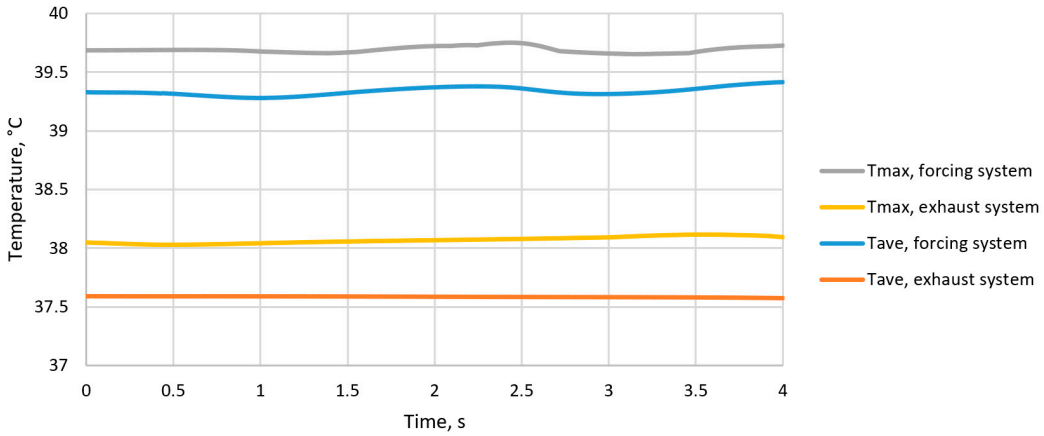

Figure 13. Maximum and average air temperatures in the area around the driver's cabin of the BM for two considered auxiliary ventilation systems.

This observation aligns well with the field data in Figure 6, which shows that a significant temperature decrease occurs only after several minutes, whereas the shuttle car moves away from the dead-end mine working in just over a minute.

The obtained results confirm our suggestion that the movement of the shuttle car, modeled using the dynamic mesh approach, primarily affects the velocity field near the BM. In contrast, temperature changes around the BM cabin are mainly driven by the gradual cooling of the BM after it is switched off. The exponential decline of the temperature curves in Figure 6 further supports this conclusion.

The cooling of mining equipment after shutdown follows an exponential pattern [40]. This can be physically interpreted in two ways. First, it is known that heat is transferred from a homogeneous heated body with heat capacity C to the surrounding airflow, governed by an effective heat transfer coefficient, h [41,42].

$$C\frac{dT}{dt} = h(T_a - T) \tag{17}$$

where T is the temperature of the mining equipment, in °C; T_a is the temperature of the air, in °C; and t is the time, in s.

The cooling of the air space in a dead-end working after the introduction of cold air also follows an exponential law. This follows from the law of mass balance, which in this case can be expressed as follows. The cold air volume Qdt with temperature T_{in}, supplied to the working area during time dt, mixes with the heated air, which has a temperature $T > T_{in}$ and occupies a part of the total volume V (volume of the airspace in the working area). As a result, the mean temperature T decreases by dT. Consequently, the incoming cold air replaces an equal volume Qdt of heated air with a new mean temperature of $T - dT$. In mathematical form, this can be written as follows:

$$T_{in}Qdt + VT = V(T - dT) + Qdt(T - dT) \tag{18}$$

or

$$\frac{dT}{dt} = \frac{Q}{V}(T_{in} - T) \tag{19}$$

The solution of Equation (19), like the solution of Equation (17), is an exponential function, and given that the order of magnitude of Q/V is about 10^{-2}, Equation (19) just gives the cooling time from some initial warm temperature $T(0)$ to the inlet temperature T_{in} in a time of about ten minutes.

4. Conclusions

In this work, a model of non-isothermal airflow in a dead-end mine working, with an operating borer miner and a moving shuttle car, was constructed and validated. The numerical solution obtained using ANSYS Fluent enabled a theoretical analysis of the heat and mass transfer patterns in the dead-end mine working under varying borer miner operating modes.

The analysis considered two extreme scenarios: one with the borer miner operating and one without. The results show that the operating mode of the borer miner significantly affects the velocity and temperature fields in the mine working, particularly in the area near the driver's cabin. This influence is due to both the switching on/off of the borer miner's cooling system and the movement of the shuttle car.

The model confirmed the experimentally observed twofold decrease in maximum speed near the borer miner cabin after the shuttle car departed. Simulation results for forcing ventilation showed a temperature difference of about 1–1.5 °C between the two extreme scenarios. The temperature field near the cabin with the exhaust ventilation system was less dependent on the presence of the shuttle car and the operation of the borer miner's cooling system. The temperature increase after turning on the borer miner's cooling system and the arrival of the shuttle car was no more than half a degree.

Unsteady simulations using the dynamic mesh approach showed that temperature variations were mainly caused by the borer miner's cooling system, while the moving shuttle car generated only short-term aerodynamic oscillations in the airspace.

The analysis confirms that the dynamic mesh approach is particularly effective for assessing the impact of a moving shuttle car on aerodynamic processes over short time intervals in dead-end mine working ventilation. Airflows around mining equipment are highly uneven, and the movement of this equipment significantly alters the air velocity field.

Author Contributions: Conceptualization, L.L., M.S. and S.M.; methodology, M.S. and R.L.; software, R.L.; validation, M.S., R.L. and A.S.; formal analysis, M.S. and A.S.; investigation, M.S., R.L. and A.S.; resources, L.L. and S.M.; data curation, L.L. and S.M.; writing—original draft preparation, M.S. and R.L.; writing—review and editing, L.L., S.M. and A.S.; visualization, R.L.; supervision, L.L. and M.S.;

project administration, L.L.; funding acquisition, L.L., M.S. and A.S. All authors have read and agreed to the published version of the manuscript.

Funding: The work was carried out as part of a major scientific project funded by the Ministry of Science and Higher Education of the Russian Federation (Agreement No. 075-15-2024-535 dated 23 April 2024).

Data Availability Statement: Data is contained within the article.

Conflicts of Interest: The authors declare no conflicts of interest.

References

1. Liu, L.; Liu, J.; Zhou, Q.; Huang, D. Machine learning algorithm selection for windage alteration fault diagnosis of mine ventilation system. *Adv. Eng. Inform.* **2022**, *53*, 101666. [CrossRef]
2. Semin, M.; Kormshchikov, D. Application of artificial intelligence in mine ventilation: A brief review. *Front. Artif. Intell.* **2024**, *7*, 1402555. [CrossRef] [PubMed]
3. Wallace, K.; Prosser, B.; Stinnette, J.D. The practice of mine ventilation engineering. *Int. J. Min. Sci. Technol.* **2015**, *25*, 165–169. [CrossRef]
4. Semin, M.; Ivantsov, A.; Lyubimova, T.; Isaevich, A.; Sukhanov, A. Analyzing the impact of heat emissions from the borer miner on the efficiency of the exhaust ventilation system in a blind heading. *Int. J. Heat Mass Transf.* **2024**, *235*, 126183. [CrossRef]
5. Brodny, J.; Tutak, M. Applying computational fluid dynamics in research on ventilation safety during underground hard coal mining: A systematic literature review. *Process. Saf. Environ. Prot.* **2021**, *151*, 373–400. [CrossRef]
6. Ahmadi, M.H.; Hekmat, M.H. Numerical and experimental investigation of air flow behavior and H2S gas emission through an inclined traversed tunnel. *J. Braz. Soc. Mech. Sci. Eng.* **2021**, *43*, 1–15. [CrossRef]
7. Adjiski, V.; Mirakovski, D.; Despodov, Z.; Mijalkovski, S. Detemining optimal distance from outlet of auxiliary forcing ventilation system to development of heading in underground mines. *J. Min. Environ.* **2019**, *10*, 821–832.
8. Obracaj, D.; Korzec, M.; Deszcz, P. Study on Methane Distribution in the Face Zone of the Fully Mechanized Roadway with Overlap Auxiliary Ventilation System. *Energies* **2021**, *14*, 6379. [CrossRef]
9. Li, Z.; Zhao, S.; Li, R.; Huang, Y.; Xu, Y.; Song, P. Increasing Oxygen Mass Fraction in Blind Headings of a Plateau Metal Mine by Oxygen Supply Duct Design: A CFD Modelling Approach. *Math. Probl. Eng.* **2020**, *2020*, 6379. [CrossRef]
10. Yi, H.; Kim, M.; Lee, D.; Park, J. Applications of Computational Fluid Dynamics for Mine Ventilation in Mineral Development. *Energies* **2022**, *15*, 8405. [CrossRef]
11. Branny, M.; Jaszczur, M.; Wodziak, W.; Szmyd, J. Experimental and numerical analysis of air flow in a dead-end channel. *J. Phys. Conf. Ser.* **2016**, *745*, 032045. [CrossRef]
12. Kurnia, J.C.; Sasmito, A.P.; Mujumdar, A.S. CFD simulation of methane dispersion and innovative methane management in underground mining faces. *Appl. Math. Model.* **2014**, *38*, 3467–3484. [CrossRef]
13. Salami, O.B.; Kumar, A.R.; Aamir, I.; Pushparaj, R.I.; Xu, G. Enhancing fire safety in underground mines: Ex-perimental and large eddy simulation of temperature attenuation, gas evolution, and bifurcation influence for improved emergency response. *Process Saf. Environ. Prot.* **2024**, *183*, 260–273. [CrossRef]
14. Fernández-Alaiz, F.; Castañón, A.M.; Gómez-Fernández, F.; Bascompta, M. Mine Fire Behavior under Different Ventilation Conditions: Real-Scale Tests and CFD Modeling. *Appl. Sci.* **2020**, *10*, 3380. [CrossRef]
15. Chung, D.; McKEON, B.J. Large-eddy simulation of large-scale structures in long channel flow. *J. Fluid Mech.* **2010**, *661*, 341–364. [CrossRef]
16. Roghanchi, P.; Kocsis, K.C. Improving the climatic conditions in development and production workings of hot underground mines by re-designing the auxiliary ventilation system: A case study. *Int. J. Min. Miner. Eng.* **2017**, *8*, 280–293. [CrossRef]
17. Hargreaves, D.; Lowndes, I. The computational modeling of the ventilation flows within a rapid development drivage. *Tunn. Undergr. Space Technol.* **2006**, *22*, 150–160. [CrossRef]
18. Isaevich, A.; Semin, M.; Levin, L.; Ivantsov, A.; Lyubimova, T. Study on the Dust Content in Dead-End Drifts in the Potash Mines for Various Ventilation Modes. *Sustainability* **2022**, *14*, 3030. [CrossRef]
19. Xin, S.; Wang, W.; Zhang, N.; Zhang, C.; Yuan, S.; Li, H.; Yang, W. Comparative studies on control of thermal environment in development headings using force/exhaust overlap ventilation systems. *J. Build. Eng.* **2021**, *38*, 102227. [CrossRef]
20. Huang, R.; Shen, X.; Wang, B.; Liao, X. Migration characteristics of CO under forced ventilation after excavation roadway blasting: A case study in a plateau mine. *J. Clean. Prod.* **2020**, *267*, 122094. [CrossRef]
21. Tutak, M.; Brodny, J. Analysis of the Impact of Auxiliary Ventilation Equipment on the Distribution and Concentration of Methane in the Tailgate. *Energies* **2018**, *11*, 3076. [CrossRef]

22. Zhang, W.; Xue, S.; Tu, Q.; Shi, G.; Zhu, Y. Study on the distribution characteristics of dust with different particle sizes under forced ventilation in a heading face. *Powder Technol.* **2022**, *406*, 117504. [CrossRef]
23. Chang, P.; Xu, G.; Zhou, F.; Mullins, B.; Abishek, S.; Chalmers, D. Minimizing DPM pollution in an underground mine by optimizing auxiliary ventilation systems using CFD. *Tunn. Undergr. Space Technol.* **2019**, *87*, 112–121. [CrossRef]
24. Xin, S.; Han, X.; Li, S.; Xiao, Y.; Yang, W. Application of Data Envelopment Analysis in the Ventilation and Cooling Efficiency Evaluation of Hot Development Headings. *Processes* **2022**, *10*, 1375. [CrossRef]
25. Olkhovsky, D.; Zaitsev, A.; Bublik, S. Study on the influence of radiation heat transfer on microclimatic parameters in the blind heading of a deep potash mine. *Int. J. Therm. Sci.* **2024**, *199*, 108904. [CrossRef]
26. Wang, Z.; Li, S.; Ren, T.; Wu, J.; Lin, H.; Shuang, H. Respirable dust pollution characteristics within an underground heading face driven with continuous miner—A CFD modelling approach. *J. Clean. Prod.* **2019**, *217*, 267–283. [CrossRef]
27. Sahu, A.; Mishra, D.P. Coal dust monitoring and computational simulations of dust dispersion in continuous miner development heading through auxiliary ventilation systems. *Curr. Sci.* **2022**, *122*, 419–428. [CrossRef]
28. Torno, S.; Toraño, J.; Ulecia, M.; Allende, C. Conventional and numerical models of blasting gas behaviour in auxiliary ventilation of mining headings. *Tunn. Undergr. Space Technol.* **2013**, *34*, 73–81. [CrossRef]
29. Zaitsev, A.; Parshakov, O.; Semin, M. Heat Emissions from Mining Machinery: Implications for Microclimatic Conditions in Underground Workings. *Mining* **2024**, *4*, 1075–1092. [CrossRef]
30. Chowdhury, I.A. State-of-the-Art CFD Simulation: A Review of Techniques, Validation Methods, and Application Scenarios. *J. Recent Trends Mech.* **2024**, *9*, 45–53. [CrossRef]
31. Wu, R.; Zhu, Z.; Cao, G. Computational Fluid Dynamics Modeling of Rope-Guided Conveyances in Two Typical Kinds of Shaft Layouts. *PLoS ONE* **2015**, *10*, e0118268. [CrossRef] [PubMed]
32. Chen, X.; Zhang, H.; Ge, S.; Deng, C.; Fan, C.; Ma, G.; Li, W. Research on the Dust Diffusion and Pollution Behaviour of Dynamic Tunneling in Header Excavators Based on Dynamic Mesh Technology and Field Measurement. *Energies* **2022**, *15*, 8945. [CrossRef]
33. Zhang, L.; Che, D. Turbulence Models for Fluid Flow and Heat Transfer Between Cross-Corrugated Plates. *Numer. Heat Transfer Part A Appl.* **2011**, *60*, 410–440. [CrossRef]
34. Churchill, S.W. A Reinterpretation of the Turbulent Prandtl Number. *Ind. Eng. Chem. Res.* **2002**, *41*, 6393–6401. [CrossRef]
35. Kays, W.M. Turbulent Prandtl number. Where are we? *ASME J. Heat Transf.* **1994**, *116*, 284–295. [CrossRef]
36. Roy, S.; Pathak, U.; Sinha, K. Variable Turbulent Prandtl Number Model for Shock/Boundary-Layer Interaction. *AIAA J.* **2018**, *56*, 342–355. [CrossRef]
37. Mrinal, K.R.; Siddique, H.; Samad, A. A Transient 3D CFD Model of a Progressive Cavity Pump. ASME Turbo Expo 2016: Turbomachinery Technical Conference and Exposition. A transient 3D CFD model of a progressive cavity pump. In *Turbo Expo: Power for Land, Sea, and Air*; American Society of Mechanical Engineers: New York, NY, USA, 2016; Volume 49873, p. V009T24A009.
38. *ANSYS Fluent Theory Guide, Release 18.0*; Ansys. Inc.: Canonsburg, PA, USA, 2017.
39. Zhou, H.; Zhong, K.; Jia, H.; Kang, Y. Analysis of the effects of dynamic mesh update method on simulating indoor airflow induced by moving objects. *Build. Environ.* **2022**, *212*, 108782. [CrossRef]
40. Perestoronin, M.P.; Zaitsev, A.V.; Semin, M.A.; Borodavkin, D.A. Experimental study of transient thermal conditions in longwall faces. *Gorn. Nauk. Tekhnologii (Min. Sci. Technol.)* **2022**, *7*, 37–48. [CrossRef]
41. Parmar, M.; Hayhurst, A. The heat transfer coefficient for a freely moving sphere in a bubbling fluidised bed. *Chem. Eng. Sci.* **2002**, *57*, 3485–3494. [CrossRef]
42. Kwaśniowski, S. Problems of Heat Transfer Modelling in Cooling Systems of Earthmoving Machinery. In *Mining Machines and Earth-Moving Equipment*; Springer: Cham, Switzerland, 2020. [CrossRef]

Disclaimer/Publisher's Note: The statements, opinions and data contained in all publications are solely those of the individual author(s) and contributor(s) and not of MDPI and/or the editor(s). MDPI and/or the editor(s) disclaim responsibility for any injury to people or property resulting from any ideas, methods, instructions or products referred to in the content.